Biomass and Bioenergy 142 (2020) 105731

Contents lists available at ScienceDirect

Biomass and Bioenergy

journal homepage: http://www.elsevier.com/locate/biombioe

Research paper

An emissions-based fuel mass loss measurement for wood-fired hydronic heaters

Joshua M. Weisberger, Joseph P. Richter, Joseph C. Mollendorf, Paul E. DesJardin *

Department of Mechanical and Aerospace Engineering, University at Buffalo, The State University of New York, Buffalo, NY, 14260-4400, United States

ARTICLE INFO

Keywords:
biomass
Combustion
Fuel mass measurement
Non-intrusive
Emissions

ABSTRACT

Regulations that standardize the evaluation of wood-fired hydronic heaters (WHH) use mass loss as an important variable to compute energy input. Generally, mass loss is measured by placing the entire appliance on a scale and measuring the system mass change. This method suffers from resolution problems since the change in mass of the fuel during a run is much smaller than the total mass of the empty appliance. This experimental study provides a higher-resolution measurement of mass loss by measuring the concentration of flue gas emissions in addition to the flow rate of air into the WHH. Three fuels (red oak, cherry, and pine) are independently tested, and measurements of the emissions are made using both a Testo gas analyzer and tunable diode laser absorption spectroscopy. A simultaneous direct measurement of the mass loss is performed using a hanging basket inside the WHH, and the average percent difference between the two methods are 5.4% for red oak, 5.4% for cherry, and 8% for pine, indicating that the emissions-based method is suitable for mass loss measurements.

1. Introduction

Biomass fuels are an important renewable source of energy for people worldwide; it has been estimated that over three billion people rely on biomass and other traditional solid fuels for cooking and heating [1]. The advantage of using biomass for these applications has been widely discussed [2–6], with many developing nations relying exclusively on biomass for energy production. Increasingly, individual households in Europe and North America are turning to single residential heaters as a means of heating and storing water, particularly in more rural regions. It is expected that the number of residential heaters will continue to increase, as in many cases, countries are providing subsidies or other incentives for their use [7–9]. Wood stove replacement campaigns, where older non-certified stoves are replaced with newer certified stoves, have had wide success in the US and Canada. Much effort is being placed into the expansion and improvement of the biomass heater industry; for example, in 2019 the U.S. Department of Energy awarded $3 million for research and development of wood stoves.

As home appliance use increases, two major concerns have arisen related to the burning of biomass fuels in residential heaters: health and air pollution. Particulate matter with diameters up to 10 μm are an indicator of poor air quality, and particulates with diameters up to 2.5 μm can have substantial impacts on respiratory and cardiovascular health as they can penetrate into the lungs [1,8]. Thousands of premature deaths per year in Europe and North America alone are attributed to heating with wood and coal. To reduce the harmful effects of using residential heaters, regulatory measures have been enacted in the EU and North America to limit particulate (and CO) emissions and increase heating efficiency. To provide stricter guidelines on the certification of biomass-burning appliances in the United States, the Environmental Protection Agency (EPA) has defined specific new regulations for wood burning appliances including wood stoves, masonry heaters, pellet-burning stoves, and hydronic heaters [10,11].

The EPA Method 28 (EPA M28) guidelines for wood-fired hydronic heaters (WHH) was instituted as a method of certifying these appliances in regards to particulate emissions and overall efficiency, and providing guidelines and comparisons for buyers to have access to when purchasing a new unit [11]. When searching for approved/certified heaters, potential buyers can compare metrics such as efficiency, emission rates, and carbon monoxide values. The efficiency in this method is defined as the percentage of the heat transferred to the space when a load of fuel is burned (or the energy output divided by the energy input). This is very similar to the Canadian standard CSA B-415, which includes many of the same measurement techniques and required resolution/accuracy limits [12]. Particulate matter emissions are measured from a wood heater burning a prepared sample of fuel in a regulated test facility. Specific procedures for determining the burn rates and particulate emission

* Corresponding author.
E-mail address: ped3@buffalo.edu (P.E. DesJardin).

https://doi.org/10.1016/j.biombioe.2020.105731
Received 19 December 2019; Received in revised form 28 July 2020; Accepted 4 August 2020
Available online 12 September 2020
0961-9534/

Nomenclature

a_i	Saturation pressure equation constants
P_c	Reference pressure [MPa]
P_s	Saturation water vapor pressure [MPa]
t	Time [hr]
t_n	Normalized time
T	Ambient temperature [K]
T_c	Reference temperature [K]
$\dot{m}_a$	Blower air flow rate [kg·hr^{-1}]
$m_f(t)$	Fuel mass at time t [kg]
$\dot{m}_f$	Fuel mass loss rate [kg·hr^{-1}]
MW	Molecular weight [kg·kmol^{-1}]
N	Moles
X	Mole fraction
γ	Moisture coefficient
μ	Mean release ratio
τ	Temperature ratio

Acronyms

BRM	Burn rate monitor
DAS	Direct absorption spectroscopy
EPA	Environmental Protection Agency
HITRAN	High-resolution transmission molecular absorption database
LBL	Line-by-line
TDLAS	Tunable diode laser absorption spectroscopy
WHH	Wood-fired hydronic heater
WMS	Wavelength modulation spectroscopy

rates, and for reducing data are provided in the standards. The burn rate is the rate at which the test fuel is consumed in a wood heater, and is measured in kg of wood per hour on a dry basis. In EPA M28, a platform scale is used for monitoring the fuel load weight change, and should be capable of measuring weight to within ±0.05 kg or 1% of the initial test fuel charge weight, whichever is greater. The same resolution is dictated in the CSA B-415 standard, but does not specify the device to make the measurement, leaving a door open for other methods of mass measurement [12]. Data is recorded at intervals no greater than 10 min, and runs are considered completed when the scale measures 0 kg for 30 s. In a review of the EPA M28 standard, it was suggested to increase data acquisition to an interval of less than 15 s [10]. One reason for the review was that many of the tested (and previously certified) appliances were obtaining efficiencies greater than those allowed by a thermodynamic analysis of the systems. The efficiency is partly based on the energy input, which is calculated using the heating value of the wood and the amount of wood consumed based on the change in mass of the appliance during a test. After noticing efficiency discrepancies, the current measurements were compared to the stack loss method, which uses the flue gas temperature, CO_2 concentration, and fuel burn rate during each reported time interval (time step) to calculate a thermodynamic-limited efficiency value. Another use of the fuel burn rate in these standards is to group the appliances into categories for testing various control settings under different loads [11,12].

Fuel mass is generally measured with two different methods. The first method is to calculate the carbon emitted by the fuel, and to then convert this value to the mass of fuel burned by using the fuel composition determined from an ultimate and proximate analysis [13]. This method is only feasible if the ultimate and proximate analyses of the fuel can be performed, and with knowledge of the mass flow rate of the emissions. The second method is to simply place the entire appliance on a scale or load cell [10–12,14,15]. While simpler than the first method, the appliance must be completely isolated from any fixed connections, including flexible connections that can expand and contract with the heating cycles, which can increase the complexity of the setup. A third method is proposed in this study, which uses mainly emissions gas measurements to infer mass. When measuring the mass using emissions measurements, the appliance can be fixed to the ground, with rigid connections to pipes, tubing, and the exhaust flue. In order to avoid affecting the flow of the gases in the chambers of the appliance, it is desirable to have a non-intrusive measurement. By probing the gas in the flue (after gases have exited the appliance), any influence of the measurement on the flow in the appliance is minimized. Using a truly non-intrusive diagnostic such as absorption measurements ensures that there is no interference of the flow. While some recent studies have used hydronic heaters to analyze particulate matter and overall heating benefits, to the authors' knowledge there has been little research conducted on non-intrusive measurements of fuel mass and burn rate of hydronic heaters [13,16–18].

This study describes a method of obtaining the instantaneous fuel mass and fuel burn rate by non-intrusively measuring flue gas emissions and the air flow rate introduced into a WHH. The emission concentrations are measured in the flue using two devices: a hand-held Testo gas analyzer measures CO, NO, and O_2, while an absorption spectroscopy system measures CO_2 and H_2O. A global, single-step reaction is used to compute the carbon-normalized fuel composition at a rate of 2 Hz over the duration of a multi-hour run for three different fuels. By also measuring the air flow rate introduced into the WHH, the fuel mass loss rate (burn rate) is calculated. After integrating the burn rate curve in time, the instantaneous fuel mass at any point during the run can be obtained. This fuel mass is then compared to the results from a hanging basket resting on a load cell (discussed later and shown in Fig. 3), which directly (but intrusively) measures the fuel mass. The time derivative of the fuel mass from the hanging basket measurement is used to obtain the fuel burn rate, and to compare to the emissions-based measurement. The methods outlined in this study can be used to supplement the existing fuel mass and burn rate measurements in use.

Section 2 presents a global, single-step reaction that can be used to compute the instantaneous carbon-normalized fuel composition, and thus the fuel mass and burn rate. Section 3 details the WHH and the fuels used, along with measurements of the direct fuel mass, emissions, and air flow rate. Section 4 discusses the results of the three fuels tested, culminating in a comparison of the direct and measured fuel mass and burn rate. Finally, Section 5 summarizes the major conclusions.

2. Fuel mass loss rate model formulation

A global, single-step reaction model is proposed to calculate the real-time, carbon-normalized fuel composition, shown in Eq. (1). The model uses *in situ* measured concentrations of emission species in the flue gas. NO_x emissions have been found to be directly related to fuel nitrogen content, so in this study the nitrogen originating in the fuel is assumed to only be converted to NO in the products [19–21]. The moisture bound in the fuel is included in the fuel composition, and the ambient air is assumed to consist of 21% O_2 and 79% N_2 by volume, with trace elements ignored due to their negligible contribution to the calculated burn rate and mass loss (e.g. ambient CO_2). Note also that the apparent fuel takes into account both bound and unbound hydrogen.

$$\begin{aligned} &C_1H_xO_yN_z + a\,(O_2 + 3.76\,N_2 + \gamma\,H_2O) \rightarrow \\ &c\,H_2O + d\,CO + e CO_2 + 3.76\,a\,N_2 + g\,O_2 + z\,NO \end{aligned} \tag{1}$$

The atom balances and measured-value equations are detailed in Eq. (2). A Testo gas analyzer is used to measure the concentrations of CO, NO, and O_2, while tunable diode laser absorption spectroscopy (TDLAS)

is used to measure the concentrations of CO_2 and H_2O.

(a) Atom balance for C : $1 = d + e$ (2)

(b) Atom balance for H : $0 = x + 2\gamma a - 2c$

(c) Atom balance for O : $0 = y - z + a(2+\gamma) - c - d - 2e - 2g$

(d) Measured using Testo : $0 = X_{CO} N_{tot} - d$

(e) Measured using Testo : $0 = X_{NO} N_{tot} - z$

(f) Measured using Testo : $0 = X_{O_2} N_{tot} - g$

(g) Measured using TDLAS : $0 = X_{CO_2} N_{tot} - e$

(h) Measured using TDLAS : $0 = X_{H_2O} N_{tot} - c$

(i) Molar conservation : $0 = N_{tot} - c - d - e - 3.76a - g - z$

Equations (a) through (c) are the atom balances for carbon, hydrogen, and oxygen. Equations (d) through (f) are the Testo-measured CO, NO, and O_2 concentrations in the flue. Equations (g) and (h) are the TDLAS-measured concentrations of CO_2 and H_2O, and equation (i) is a molar conservation equation. Equations (d) through (h) constitute the five emissions measurements. In total, nine equations are solved and are expressed in matrix form in Eq. (3).

$$\begin{bmatrix} 0 & 0 & 0 & 0 & 0 & 1 & 1 & 0 & 0 \\ 1 & 0 & 0 & 2\gamma & -2 & 0 & 0 & 0 & 0 \\ 0 & 1 & -1 & (2+\gamma) & -1 & -1 & -2 & -2 & 0 \\ 0 & 0 & 0 & 0 & 0 & -1 & 0 & 0 & X_{CO} \\ 0 & 0 & -1 & 0 & 0 & 0 & 0 & 0 & X_{NO} \\ 0 & 0 & 0 & 0 & 0 & 0 & 0 & -1 & X_{O_2} \\ 0 & 0 & 0 & 0 & 0 & 0 & -1 & 0 & X_{CO_2} \\ 0 & 0 & 0 & 0 & -1 & 0 & 0 & 0 & X_{H_2O} \\ 0 & 0 & -1 & -3.76 & -1 & -1 & -1 & -1 & 1 \end{bmatrix} \begin{bmatrix} x \\ y \\ z \\ a \\ c \\ d \\ e \\ g \\ N_{tot} \end{bmatrix} = \begin{bmatrix} 1 \\ 0 \\ 0 \\ 0 \\ 0 \\ 0 \\ 0 \\ 0 \\ 0 \end{bmatrix} \quad (3)$$

The variable γ is the moisture coefficient, which describes the ratio of mole fractions between water and oxygen in humid air. The ambient temperature (T) and relative humidity are first measured in the laboratory. The saturation water vapor pressure (P_s) is calculated using Eq. (4) from Wagner and Pruss [22], where the reference temperature and pressure are $T_c = 647.096$ K and $P_c = 22.064$ MPa, and the values of the constants are: $a_1 = -7.85951783$, $a_2 = 1.84408259$, $a_3 = -11.7866497$, $a_4 = 22.6807411$, $a_5 = -15.9618719$, and $a_6 = 1.80122502$. The variable τ is defined as $1 - TT_c^{-1}$ for convenience.

$$ln\left(\frac{P_s}{P_c}\right) = \frac{T_c}{T}\left[a_1\tau + a_2\tau^{1.5} + a_3\tau^3 + a_4\tau^{3.5} + a_5\tau^4 + a_6\tau^{7.5}\right] \quad (4)$$

The saturation water vapor pressure is multiplied by the relative humidity to give the actual water vapor pressure, and the mole fraction of H_2O is equal to the water vapor pressure divided by the laboratory atmospheric pressure. The "dry" O_2 mole fraction is equal to 4.76^{-1}, and the "wet" O_2 mole fraction is $(1 - X_{H_2O})X_{O_2,dry}$.

The solution of the system of equations results in H/ C (x), O/ C (y), and N/C (z) atomic ratios (carbon-normalized) of the non-homogeneously decomposing fuel. The H/O atomic ratio is computed with x/y (see discussion in Section 4.2). By measuring the blower air flow rate, $\dot{m}_a$, the fuel burn rate ($\dot{m}_f$) can be computed using Eq. (5), which incorporates the time-dependent atomic fuel composition (x, y, z) that was solved for in the previous step, along with reactant air values of a and γ.

$$\dot{m}_f = \dot{m}_a \frac{MW_C + xMW_H + yMW_O + zMW_N}{a(MW_{O_2} + 3.76MW_{N_2} + \gamma MW_{H_2O})} \quad (5)$$

Note that this model is predicated on the unit being well-sealed; that is, the only air entering the unit is from the blower with a known mass flow rate. The fuel mass loss rate is then integrated over time to calculate the instantaneous fuel mass at time t (see discussion in Section 4.3).

$$m_f(t) = \int_0^t \dot{m}_f \, dt \quad (6)$$

3. Experimental setup and diagnostics

3.1. Wood-fired hydronic heater

The tests are performed using an Econoburn EBW-200 wood-fired hydronic heater (211 MJ), a schematic of which can be seen in Fig. 1. These types of appliances are generally used to heat water which is then stored in a separate insulated tank. The water is circulated around the outer walls of the appliance (water jacket), exchanging heat with the hot gases inside. The heated water can then be used later for heating, cooking, and cleaning. For convenience, the WHH is considered in terms of three distinct sections: the primary chamber, the secondary chamber, and the water circulation loops. The fuel in the upper chamber undergoes pyrolysis and partial oxidation. While the term "pyrolysis" is used here, there is in fact air present in the upper chamber, but at levels well below stoichiometric, and so it is heavily fuel-rich. These fuel-rich products are then forced down through a rectangular orifice from the primary to the secondary chamber, mixing with secondary preheated air that is forced in through the orifice orthogonal to the downward product flow direction. The secondary chamber is used to oxidize the remaining products of combustion through turbulent mixing. The turbulent mixing of the primary-secondary jet increases the flame area resulting in more efficient burning. Before exhausting out of the WHH through the flue, the gases are further mixed through swirl-tubes on the back side of the unit that run from the secondary chamber (bottom of the WHH) to the flue exit (top of the WHH). As the gases pass from the primary chamber, through the secondary chamber, and up through the swirl-tubes, they are constantly exchanging heat with the walls that separate the chambers from the water jacket.

The WHH has two main water flow loops, shown in dashed (loop 1) and solid (loop 2) colored lines in Fig. 1. Hot and cold water are indicated with red and blue lines, respectively. Early in a run, the hot water flows around loop 1 to circulate the relatively cold water until its temperature reaches 339 K. Once this temperature is reached, loop 2 is activated by turning off pump P1 and turning on pump P2. The hot water leaving the WHH now circulates through an 87.9 kW counter-flow heat exchanger, transferring heat to the city-side cold water supply before cycling back into the water jacket. The heat rate is monitored using the water inlet and outlet temperatures using K-type thermocouples and water flow rate meters (Dwyer Instruments). When the WHH is used in a residential setting, the heat exchanger is replaced with a water storage tank.

Three criteria are defined to initiate the run shutdown procedure, all with measurements in the flue exhaust gases: the gas temperature falls below 366 K, the O_2 content is greater than 19%, and the CO concentration is less than 1000×10^{-6} m^3m^{-3} (1000 ppm). When these conditions are met, the flow rate of the city-side cold water is increased to remove as much heat as possible from the circulating water.

3.2. Fuels

Three types of fuel are used in this study in order to sample a range of chemical compositions to test the non-intrusive diagnostic method: red oak (BIOBLOCKS manufactured by Summit Wood Industries), pine, and cherry. The red oak wood comes in bricks that are made from 100% hardwood chips, and contain an average 8% dry-basis by mass moisture content (measured in accordance with ISO standard 3130). The approximate composition of red oak is $C_1H_{1.7}O_{0.72}N_{0.001}$ [23], and after including the moisture content is $C_1H_{1.94}O_{0.83}N_{0.001}$. The pine wood is obtained from a local lumber supplier and kiln-dried to 14% dry-basis by

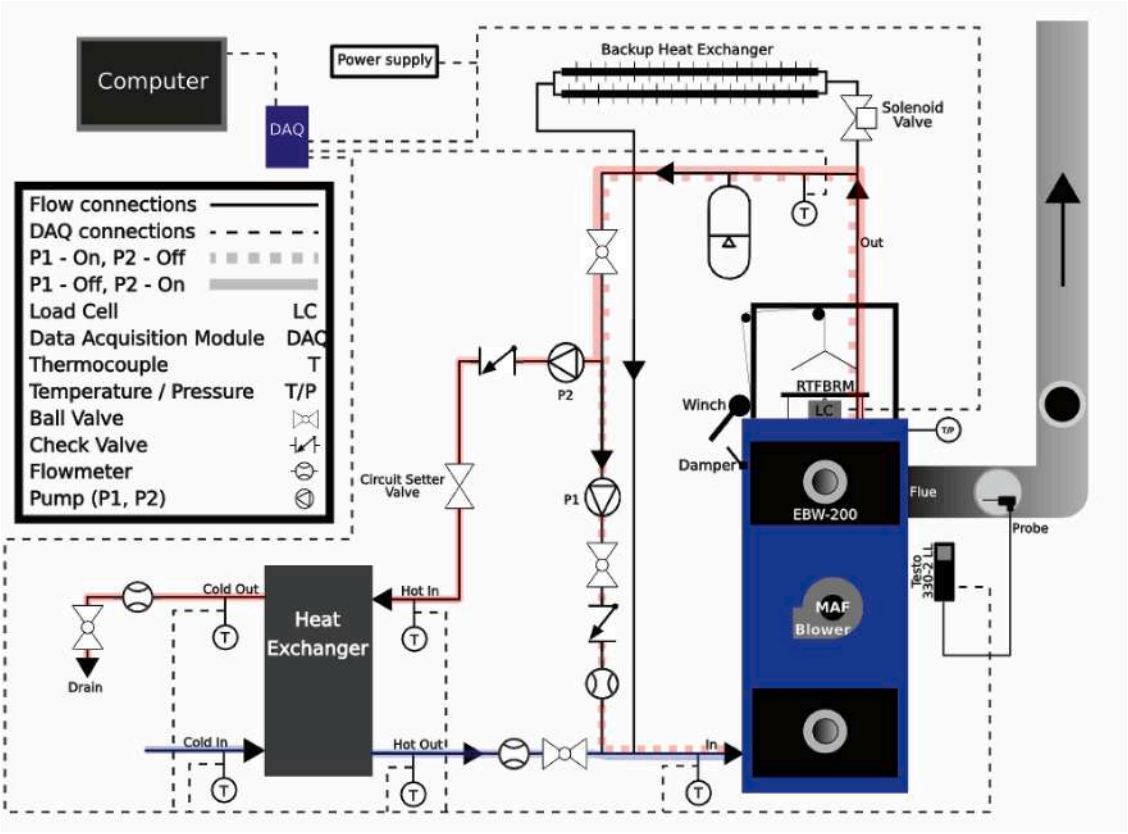

Fig. 1. Schematic of the WHH setup, including electrical connections (dashed black) and water flow loops (solid black, highlighted red for hot water and blue for cold water). (For interpretation of the references to color in this figure legend, the reader is referred to the Web version of this article.)

mass moisture content. The cherry wood is locally sourced and kiln-dried cordwood with a 15% moisture content. A Testo 606-1 moisture meter is used to measure the moisture content of the pine and cherry by averaging measurements of both end- and center-cut locations of a random sample of 20 pieces for each. While cherry is not a commonly used feedstock, it was used in these experiments to study a different fuel with a much different geometry (cherry cordwood vs. red oak/pine blocks). The testing of a wider variety of feedstocks with this method is outside the scope of the study. The dimensions of the red oak and pine blocks are $6.4 \times 10 \times 14$ cm, while the size of the cherry varies from piece to piece, but is roughly three to six times as large as the red oak or pine blocks. Ultimate analyses of red oak [23–25], cherry [25,26], and pine [20,24,25,27–29] have been performed by various authors. While the ultimate analysis of the fuel used in this study may differ slightly from these reported values, the general trends of their carbon, hydrogen, oxygen, and nitrogen atomic compositions are presumed to be similar. The H/O ratios vary from 1.96 to 2.36 for red oak, from 2.08 to 2.13 for cherry, and from 1.79 to 3.36 for pine. For wood in general, the H/O ratio varies from 2.24 to 2.41 [2,30]. The H/ O ratio for an ultimate analysis is, by definition, a constant value. In Eq. (1), however, the ratio of H to O was not fixed to a specific value. In a previous study, to reduce the number of emissions measurements needed, this ratio was assumed to be constant at a value of 2 [31]. The current study incorporates an extra emission measurement in order to allow the H and O values to be computed, which are then compared to the constant values from the ultimate analysis (see Section 4.2).

Wood fuel is loaded into the primary chamber hanging basket in the three configurations shown in Fig. 2. Fig. 2a indicates the six steps for loading fuel into the hanging basket, including the bottom layer placement (1), addition of first layer kindling (2,3), second layer of fuel (4), second layer kindling (5), and final layer of fuel (6). Loading in this configuration resulted in easily ignitable fuel charges along with repeatable runs. Due to the different fuel densities and the available hanging basket size, run mass differed from fuel to fuel. A full load for red oak consisted of 32 blocks (≈ 28 kg), for pine consisted of 32 blocks (≈ 16 kg), and for cherry consisted of approximately 16 split logs of cordwood (≈ 19 kg). The pine wood was cut into very similar dimensions as the red oak blocks, while the cherry was left in a split log geometry. The exact geometry has no influence on the calculation of the mass loss.

3.3. Direct fuel measurement

The WHH used in this study was not placed on a scale for weighing. Instead, a hanging basket burn rate monitor (BRM) in the primary chamber was used to support the fuel and measure the time varying mass throughout a run (Fig. 3) [32]. Comparisons between the emissions-based mass loss and BRM mass loss are made in Section 4.3, where the BRM data is assumed to be the true value of the fuel mass for comparisons in this study. While the hanging basket may seem like a better option for measuring fuel mass during a run, it is not an ideal solution for several reasons. First, the ideal placement of the fuel in the primary chamber is on the floor surrounding the primary-secondary orifice. The BRM raises the fuel off the floor, enabling the product gases to more easily move to the secondary chamber, reducing the completeness of the initial combustion reaction. Second, the BRM installation requires substantial modification to the WHH, including drilling into the water jacket support rods to allow the BRM through-rods to pass into the primary chamber, installing a pancake load cell (Stellar Technology) to measure the mass, thermally insulating the load cell to avoid thermal drifts, and installing a winch system to lift the basket off the load cell during fuel loading. The water jacket support rods are called *stays*, which are 2.54 cm diameter rods that support/attach the water jacket shell to the inner shell/chambers. The

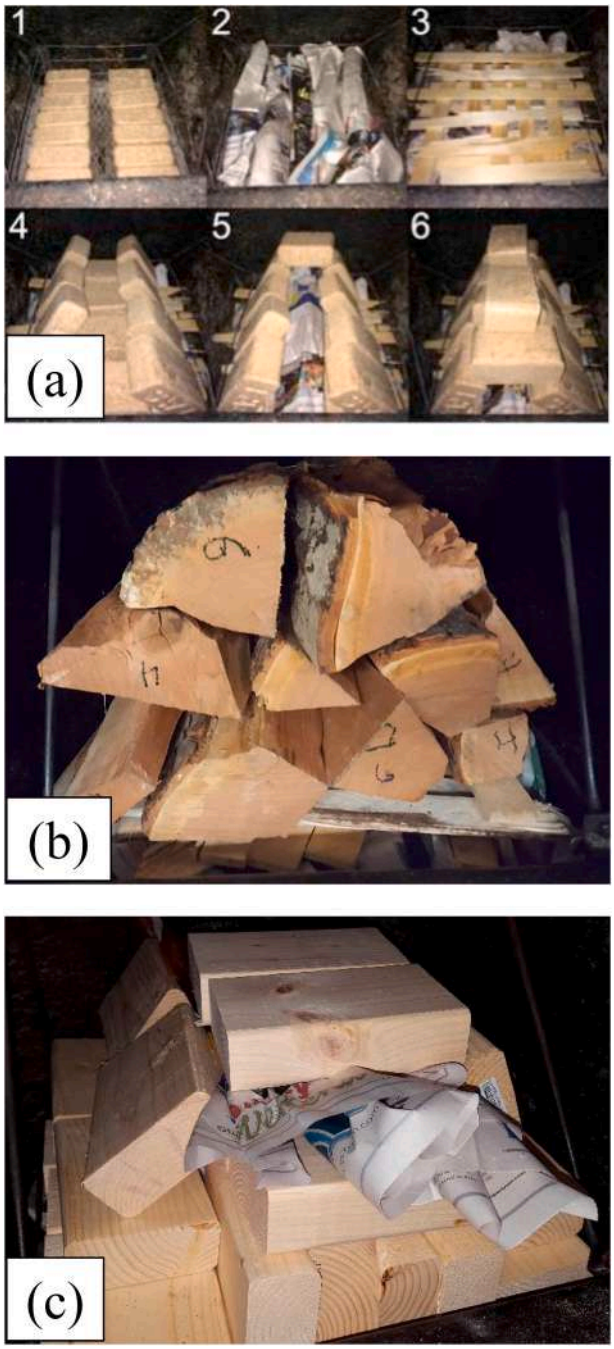

Fig. 2. Loading configurations for (a) red oak, (b) cherry, and (c) pine. (For interpretation of the references to color in this figure legend, the reader is referred to the Web version of this article.)

through-rods that pass through the stays to connect the basket to the upper cross-member (which rests on the load cell) need to be meticulously cleaned between runs to ensure they do not stick to or catch on the stays; graphite is also coated on the through-rods to minimize friction. Third, because the primary purpose of the regulatory standard testing is to improve the efficiency and lower the emissions from residential WHHs, the BRM installation would skew these results since it is an intrusive measurement. Using an emissions-based measurement provides a non-intrusive measurement, allowing the testing to be performed in exactly the way the appliance would operate at a residential home. The BRM does, however, provide a direct, accurate method with which to compare the emissions-based measurements.

3.4. Testo gas analyzer

Emissions in the exhaust flue are obtained using a Testo 330-2 L L flue gas analyzer, which measures concentrations of O_2, CO, and NO, along with pressure and temperature of the gas. The system is also capable of providing estimates of CO_2 and H_2O, but the more accurate methods of absorption spectroscopy (Section 3.5) are used in this study to determine those concentrations. The O_2, CO, and NO concentrations are all detected via an electrochemical fuel cell, but operate slightly differently. For O_2, a permeable layer of electrodes allows the flue oxygen molecules and reference air molecules to transfer ions, which creates a voltage potential that can be interpreted as an O_2 concentration of the flue gases. For CO measurements, oxygen molecules that permeate the electrodes are used to react with the CO on the opposite electrode to form CO_2, which results in the consumption of O_2 on the reference side of the fuel cell. When used in conjunction with the electrode at the reaction location, a voltage potential is obtained that can be interpreted as a concentration of CO. This unit was also equipped with H_2 -compensation and automatic fresh air dilution options. The NO sensor operates on the same principle as the CO sensor. Temperature is measured with a probe located in the flue gas probe line in order make direct measurements at the gas sampling location in the flue. Measurement ranges, resolutions, and accuracies are detailed in Table 1.

To correct measurements for water condensation in the sampling line, the correction procedure of Richter et al. [33] is used, which requires a separate measurement of O_2 using a Bosch LSU 4.9 ZrO_2 wide-band oxygen/lambda sensor. Ambient moisture content and temperature are measured with an Omega HX92B series humidity sensor and a K-type thermocouple, respectively.

3.5. Absorption spectroscopy diagnostic

Tunable diode laser absorption spectroscopy (TDLAS) is used to measure concentrations of CO_2 and H_2O in the flue exhaust stream. In TDLAS, a laser source scans over a range of wavenumbers, and at certain wavenumbers along the scan, the species of interest absorb the incident radiation. A distributed feedback diode laser centered at 2.715 μm (Nanoplus) is housed in a TO-5 heat sink housing with a collimation lens on the front. A Lightwave ILX LDC-3721 laser diode driver and thermoelectric cooler (LDD-TEC) is used to control the current and temperature to the laser. At 155 mA and 37 °C, the laser emits at 3683.24 cm^{-1}. To provide a scan over a range of wavenumbers, a Tektronix AFG3051C arbitrary waveform generator is used to ramp the injection current to the laser. By choosing the current, temperature, and ramp shape/voltage limits, the laser can scan over a desired range of wavenumbers. The scan range used for this experiment was from 3683.5 cm^{-1} to 3686.5 cm^{-1}, in which there are multiple CO_2 and H_2O absorption lines.

A schematic of the laser system is shown in Fig. 4, which operates as a pitch/catch system; the laser beam is emitted from the pitch side, passes through the absorbing gases in the flue, and the resulting transmitted signal is detected on the catch side. The laser light is depicted with dashed lines, while electrical connections are depicted with solid lines. The laser (L) emits a collimated beam, which first encounters a 50/50 beamsplitter (BS^1). Half the beam is reflected through a focusing optic (FO^1) and onto a photodiode (PD^1), which measures the non-absorbing laser intensity. The other half of the laser beam passes through BS^1 and encounters a second 50/50 beamsplitter (BS^2). The reflected beam first passes through a solid germanium etalon (E) that has a free spectral range or 0.75 GHz, then through a focusing optic (FO^2), and onto a second photodiode (PD^2). This beam provides a wavenumber calibration, which is used to transform the raw absorption data from units of time to units of wavenumber. The beam transmitted through BS^2 then passes out of the N_2 -purged housing through a plastic conduit (C^1) and an aluminum extension tube (ET^1). It then passes through a sapphire

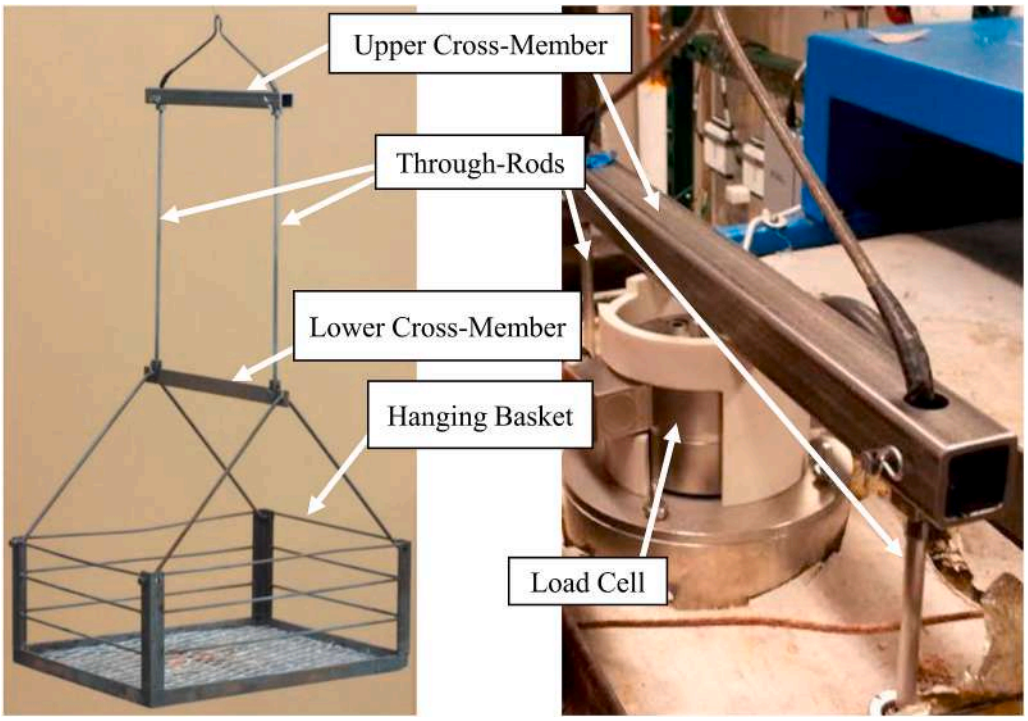

Fig. 3. Hanging basket image (left) and upper cross-member supported on top of the load cell atop the WHH (right). (For interpretation of the references to color in this figure legend, the reader is referred to the Web version of this article.)

Table 1
Testo 330-2 L L flue gas analyzer measurement range, resolution, and accuracy.

Measurement	Range	Resolution	Accuracy
O_2	0% to 21% by volume	0.1% by volume	±0.2% by volume
CO	0 to $30,000 \times 10^{-6}$ m^3m^{-3}(30,000 ppm)	1×10^{-6} m^3m^{-3}(1 ppm)	$\pm 100 \times 10^{-6}$ m^3m^{-3}(100 ppm)
NO	0 to $3,000 \times 10^{-6}$ m^3m^{-3}(3,000 ppm)	1×10^{-6} m^3m^{-3}(1 ppm)	$\pm 5 \times 10^{-6}$ m^3m^{-3}(5 ppm)
T	−40°C to 1200°C	0.1°C	±0.5°C

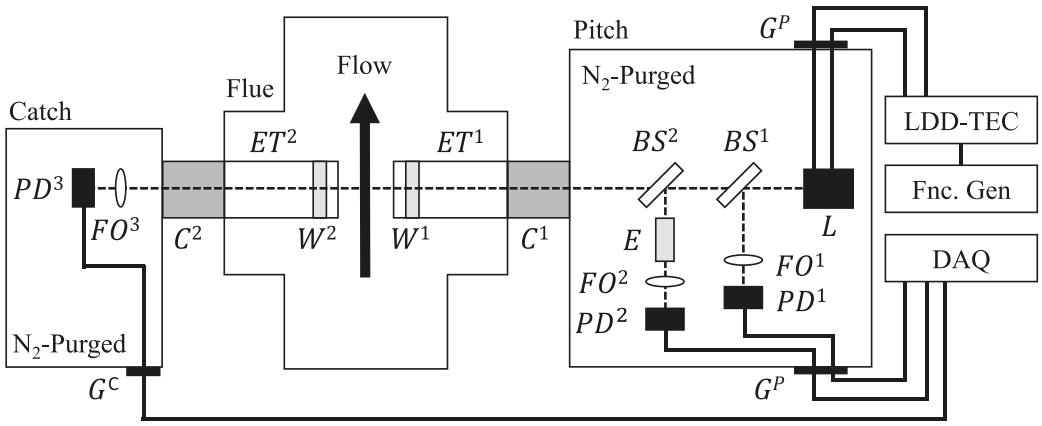

Fig. 4. Schematic of the laser absorption setup straddling the flue duct, including pitch side, catch side, nitrogen-purged boxes, laser path (dashed), and electrical connections (solid).

window (W^1) into the flue. The windows have an anti-reflection coating to prevent signal loss, and have 3 min of wedge to prevent etaloning, ensuring a linear baseline of the ramping laser intensity. The laser beam traverses the flue perpendicular to the flue gas flow such that the velocity of the flowing gases does not impart a Doppler shift on the absorption data. The beam then passes through another sapphire window (W^2), extension tube (ET^2), and conduit (C^2). The windows are recessed slightly into the extension tubes, and nitrogen gas is slowly

pumped into this recess such that soot is not able to build up on the window surfaces. The absorbing path length is then simply the distance between the ends of the extension tubes. Previous experiments verified this path length by ensuring the flow rate of the nitrogen purge gas was high enough to prevent soot buildup, but low enough to merely leak over the sides of the extension tubes, and not extend further into the absorbing path length. The laser beam, now in the N_2 - purged catch box, passes through a focusing optic (FO^3) and onto a third photodiode (PD^3); this is the absorbing signal. All three detectors are connected to a PCI-DAS4020/12 data acquisition board (Measurement Computing). Both the pitch and catch sides are housed inside acrylic boxes that are purged with N_2 such that no absorption of the beam takes place outside the flue.

After the experimental absorption data has been acquired, the data is processed with a line-by-line (LBL) absorption simulation [34], which is used to simulate the absorption spectrum over a wavenumber range (scan range of the laser), for a gas species (or multiple species), and for prescribed conditions (pressure, temperature, path length, concentration). These simulations use data from the high-resolution transmission molecular absorption database, HITRAN [35]. Both direct absorption spectroscopy (DAS) and wavelength modulation spectroscopy (WMS) are used, with the added benefit that both data sets can be taken simultaneously. WMS measurements require faster detectors and acquisition systems, but provide measurements with lower detection limits that are immune to vibrations and window fouling. DAS measurements can be performed with slow detectors and very simple acquisition systems, but the measurements are more susceptible to optical etaloning and have higher detection limits. Processing of DAS data is faster and more direct than that of WMS. Taking data for both systems simultaneously provides a check on the DAS data in regions where concentrations are sufficient for DAS, and allows the WMS to fill in the data at the lower concentration limits of the run. Details of the DAS method used in this study can be found in Ref. [36,37], which is suitable for absorption spectra where mildly-blended features are present. Results from this code were compared to a benchmark absorption code to validate the results [38]. The method for WMS analysis follows the procedure in Sun et al. [39].

The Testo gas analyzer is capable of measuring the CO_2 concentration as well, but it is estimated indirectly using the O_2 measurement and is limited by the maximum theoretical value of CO_2 based on the fuel composition at the stoichiometric limit. The fuel composition used for this measurement is set in the Testo software, and does not reflect the continuously changing composition during a run, and thus results in unreliable values; this was the reason for using the absorption measurements. It should be noted that any non-intrusive measurement can be used to measure CO_2 and H_2O, given that their quantities are verified to be accurate prior to running. For instance, in the CSA B-415 standard, it is mentioned that a continuous infrared analyzer can be used to measure flue gas emissions [12].

3.6. Air flow measurement

Air is introduced into the primary chamber by a blower pump (labeled “Blower” in Fig. 1), where the flow rate is measured using a Bosch HFM-7 mass air flow meter (using hot wire anemometry). The accuracy of the meter is typically within 3% of a known mass flow rate, and calibration of the meter is performed with an ASME standard venturi flow meter across a wide range of flow rates to correlate output voltage to the measured flow rate [40]. The major air flow rate changes during run operation are due to the appliance damper being pulled (the operating handle is shown Fig. 1). The damper is initially in an “open” position, where the exhaust gases from the primary chamber are allowed to escape unobstructed straight out to the flue through a bypass port. This “open” position is used early in the run to ensure all of the fuel is able to ignite uniformly. Once stable combustion of the fuel has been achieved, the damper is pulled into the “closed” position, which seals the bypass port. The gases are then forced to pass down into the secondary chamber and up through the mixing tubes at the back of the unit before exiting through the flue. The air flow rate measurement along with the flue gas emissions measurements are used to compute the fuel mass loss rate and instantaneous fuel mass.

4. Results and discussion

4.1. Emissions measurements

TDLAS-measured H_2O and CO_2 mole fractions are plotted in Figs. 5 and 6, respectively. In Fig. 5, the concentration increases sharply in the beginning of the run due to evaporation of the moisture bound in the fuel (evaporation phase). Next, the steady linear decline in H_2O concentration indicates the pyrolysis/combustion phase has begun, with the continuation of the drying process of the fuel. The dash-dot lines indicate the moisture level of the laboratory air that is introduced to the WHH by the blower, and are colored based on their associated fuel run. When the H_2O concentration reaches this level, charcoal oxidation (the final phase) is assumed to occur. Different fuels and different initial mass loads mean that the three phases of the run will happen over varying time durations. To collapse different fuels to the same time scale, a normalized time (t_n) is used, where the actual run time is normalized to the time at which all the fuel-bound moisture is driven from the fuel, and the moisture level is at that of the laboratory air. These values are consistent with the relative humidity reading in the laboratory for each run. The times used for normalization for each run are as follows: 2.87 hr for red oak, 2.10 hr for cherry, and 2.95 hr for pine. The CO_2 trend seen in Fig. 6 is simpler, showing an increase in CO_2 emissions, peaking at approximately $t_n = 0.5$ and then decreasing continuously until the end of the run. The increase in CO_2 concentration occurs for the drying and pyrolysis/combustion stages, and then decreases steadily for the remainder of the run in the charcoal oxidation stage. Specifically a sharp increase is seen during run start-up when the kindling uniformly ignites all the fuel. The higher CO_2 concentrations in the middle of the run, coupled with a decrease in CO, indicate more complete combustion. Uncertainty estimates for the absorption measurements are computed based on the fitting parameters used for the LBL baseline fitting procedure, as well as the spread of calculated concentrations about a mean

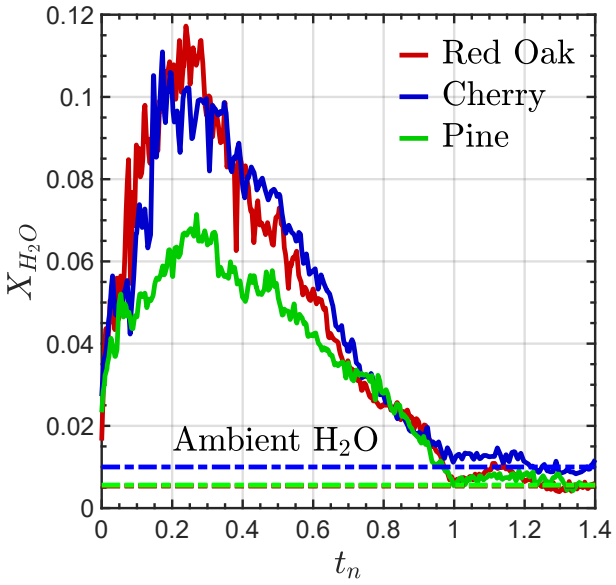

Fig. 5. H_2O concentration for three fuels as a function of normalized time, measured using absorption spectroscopy. (For interpretation of the references to color in this figure legend, the reader is referred to the Web version of this article.)

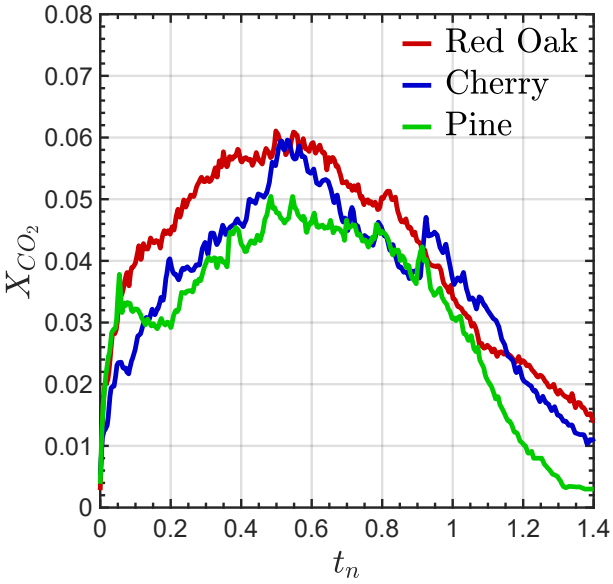

Fig. 6. CO_2 concentration for three fuels as a function of normalized time, measured using absorption spectroscopy. (For interpretation of the references to color in this figure legend, the reader is referred to the Web version of this article.)

line. An uncertainty can be calculated for each acquired data point, but trends of the uncertainties for early, middle, and late times are given here in order to avoid cluttering the figures. Uncertainties for CO_2 and H_2O mole fractions early in time are ±0.0005 and ± 0.005, middle in time are ±0.005 and ±0.015, and late in time are ± 0.002 and ± 0.005, respectively.

The Testo-measured flue O_2, CO, and NO mole fractions as a function of normalized time are shown in Figs. 7–9, respectively. In Fig. 7, the O_2 concentration first starts at values of the ambient oxygen introduced by the blower. As the combustion process ramps up, the amount of oxygen needed for combustion increases, resulting in a reduction of the O_2 at the flue. The sharp dips in the O_2 concentration before or near $t_n = 0.1$ is a result of the damper being pulled, which forces air through the

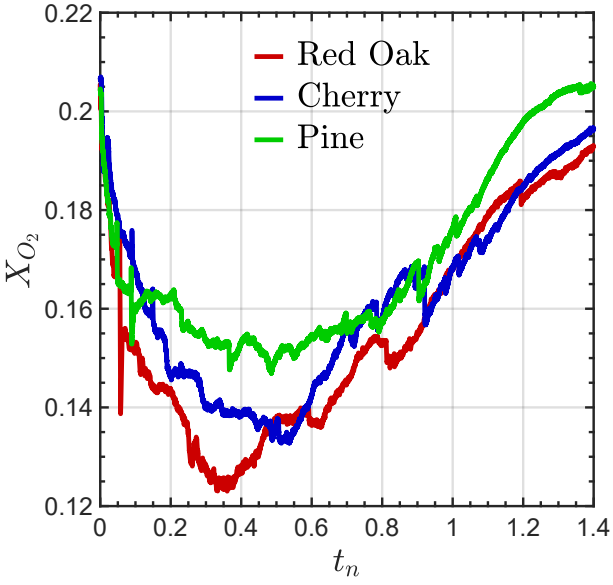

Fig. 7. O_2 concentration for three fuels as a function of normalized time, measured using Testo hand-held gas analyzer. (For interpretation of the references to color in this figure legend, the reader is referred to the Web version of this article.)

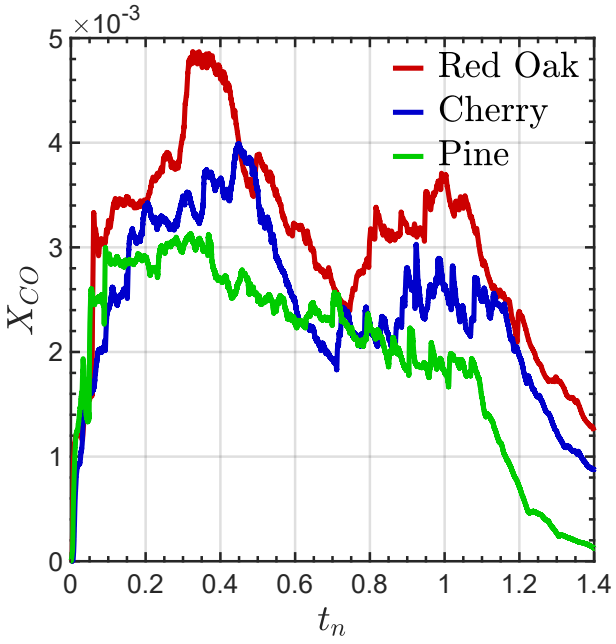

Fig. 8. CO concentration for three fuels as a function of normalized time, measured using Testo hand-held gas analyzer. (For interpretation of the references to color in this figure legend, the reader is referred to the Web version of this article.)

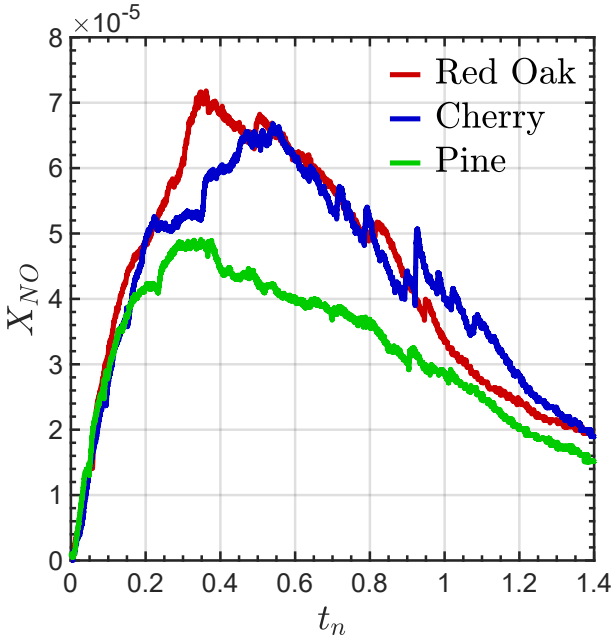

Fig. 9. NO concentration for three fuels as a function of normalized time, measured using Testo hand-held gas analyzer. (For interpretation of the references to color in this figure legend, the reader is referred to the Web version of this article.)

secondary chamber, where further combustion takes place and O_2 levels decrease further. While the peak minimum concentration levels do not occur at the same time, the trends for all three fuels are similar. Towards the end of the run, when there is less fuel with which to react, the O_2 concentrations begin to trend back to atmospheric levels. Fig. 8 shows the CO results, with the same sharp increase in concentration visible near $t_n = 0.1$ due to the damper being pulled. The red oak and cherry exhibit clear dual-peak trends, whereas the pine dual-peak is much

subtler. The dual-peak has been shown to be due to the dual-oxidation pathway description of combustion, in which the first peak is associated with pyrolysis gas burning, and the second peak corresponds to char oxidation [41]. From the discussion of Fig. 5, it was mentioned that at $t_n = 1$, charcoal oxidation was occurring. This is made clearer with the secondary peak very near $t_n = 1$. The NO trends in Fig. 9 all follow a very similar trend, with a gentle upward slope initially, where the pulled damper does not seem to have much of an impact on the resulting flue concentrations. A peak in NO emissions is reached at nearly the same time as the primary peak of the CO concentration from Fig. 8, with a continuous steady decay that follows until the end of the run.

4.2. H/O Ratio calculations

By evaluating the matrix system in Eq. (3) at every time step for which data is recorded throughout the run, the atomic ratios of H/ C and O/C are obtained and plotted for each fuel as a function of normalized time in Fig. 10. At the beginning of the run, the atomic ratios fluctuate as all the individual pieces of fuel ignite at different times. When the fuel is loaded into the primary chamber, kindling wood is placed between the layers of fuel, and when ignited, the fuel ignition is staggered depending on their proximity to the kindling. At approximately $t_n = 0.1$, the fuel is assumed to be nearly completely ignited and what follows shortly after is a quasi-steady-state release of H and O from the fuel, indicated by the nearly linear decrease in both atomic ratios. While there is no true steady-state for experiments in a WHH, the quasi-steady-state terminology used here is in reference to the development of the emissions, not of the fuel. Data after $t_n = 1$ is omitted because at this point there is no more fuel H or O. From the ultimate analyses of previous studies of red oak, cherry, and pine, the carbon-normalized atomic composition of H generally ranges from 1.3 to 1.7 (red oak), 1.4 to 1.6 (cherry), and 1.3 to 1.9 (pine). The carbon-normalized atomic composition of O generally ranges from 0.65 to 0.72 (red oak), 0.67 to 0.77 (cherry), and 0.58 to 0.77 (pine). For most of the run, the H/C and O/C ratios are well above these ranges, but at time $t_n \approx 0.7$, the values of both ratios simultaneously match quite well with the values from the ultimate analyses. Based on the propagation of uncertainties of the absorption and Testo measurements through the solution of the global reaction, uncertainties for the H/C and O/C atomic ratios are determined. Similar to the absorption measurement uncertainties, these atomic ratio uncertainties can be found at every data point, but are reported here for the three phases (drying, pyrolysis and combustion, and charcoal oxidation). For H/C, these uncertainties are large in the drying phase, ±0.25 in the pyrolysis and combustion phase, and ±0.2 in the charcoal oxidation phase. Similarly for O/C, these uncertainties are large in the drying phase, ±0.2 in the pyrolysis and combustion phase, and ±0.2 in the charcoal oxidation phase.

The H/C ratio is divided by the O/C ratio at every time step, and the resulting H/O atomic ratio is shown in Fig. 11. The first tenth of the normalized time corresponds to run start-up, which is clearer here than in Fig. 10. While the H/C and O/C atomic ratios seem to fluctuate rapidly during this phase, the ratio of H/O climbs linearly from its starting value of approximately 1.25. After the fuel combustion and pyrolysis has steadied ($t_n = 0.1$), the H and O are released from the fuel at an approximately constant ratio, until all of the H and O has been released at $t_n = 1$. At this point, the only H and O being measured in the exhaust stream is from the air introduced from the ambient laboratory by the blower.

For each fuel, the H/O release is approximately constant during the run time. By computing the mean of the H/O ratio in the range $0.1 < t_n < 1$, the mean release ratio (μ) for each fuel can be determined. The value of μ for each fuel is plotted in Fig. 11 with an appropriately colored horizontal line, where the mean release ratio for red oak is $\mu = 2.25$, for cherry is $\mu = 2.19$, and for pine is $\mu = 2.42$. Uncertainties early in the run time ($0 < t_n < 0.1$) are large and the H/O data is not included in the calculation of μ. In the range of calculations ($0.1 < t_n < 1$), uncertainties in the value of μ range from approximately ±0.25 to ±0.32 for all fuels, since these values can be calculated at every data point during a run. A previous study has assumed a mean release ratio of $\mu = 2$ [32], and the results in the current study support that this is generally a reasonable approximation. The $\mu \approx 2$ assumption can be used if, for example, measurements of CO_2 and H_2O cannot be made. Note that after all of the H and O are released from the fuel ($t_n = 1$), the mean release ratio loses meaning. However, if using a constant value of μ in the analysis, the value can be used for the entire run duration because it will have no impact on the results after all the H and O are released from the fuel.

Comparisons can be made between the H/O ratio measured in this study with those of ultimate analyses. The value of μ for red oak varies

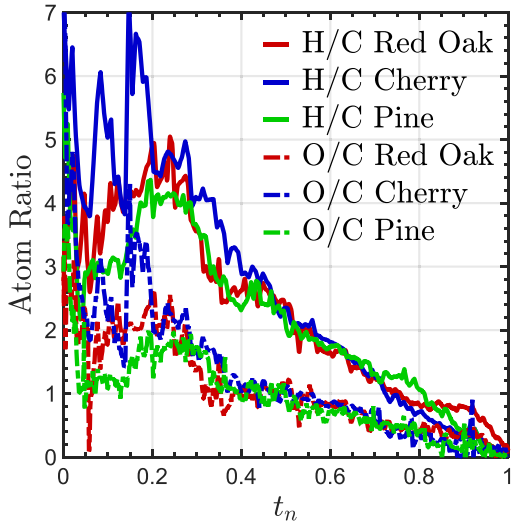

Fig. 10. H/C (solid) and O/C (dash-dot) ratio for all runs as a function of normalized time. (For interpretation of the references to color in this figure legend, the reader is referred to the Web version of this article.)

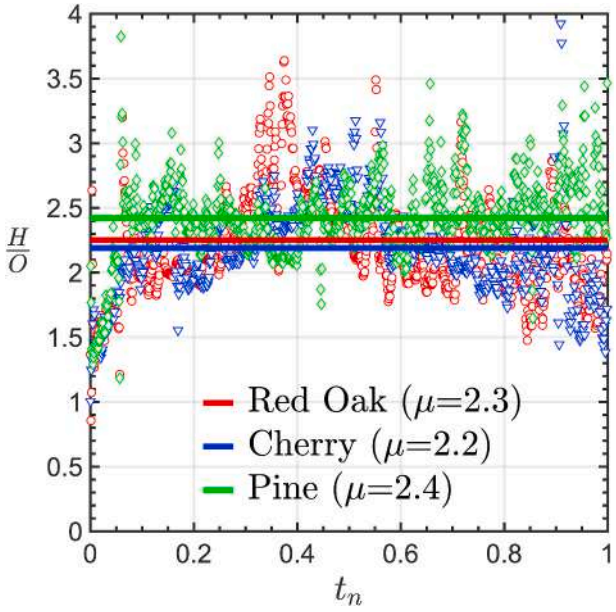

Fig. 11. H/O ratio for three fuels as a function of normalized time, with mean release ratio μ for each fuel computed between $t_n = 0.1$ and $t_n = 1$ (solid). (For interpretation of the references to color in this figure legend, the reader is referred to the Web version of this article.)

between 1.96 and 2.36 [23–25], for cherry is approximately equal to 2.1 [25,26], and for pine varies between 1.79 and 2.25 [20,24,25,28]. If an ultimate analysis of the fuel is performed prior to a run, it is then reasonable to assume that the H/O ratio from that analysis can be used as the value of μ. While an ultimate analysis of the fuels in this study was not performed, future testing will include these measurements to compare to the measured mean release ratio to further validate this assumption.

4.3. Mass loss and fuel burn rate

At every data acquisition time step during the run, the results from the solution of Eq. (3) and the air flow rate from the blower are used to compute the fuel mass loss rate (burn rate) using Eq. (5). The burn rate from the emissions measurements is then integrated in time to calculate the instantaneous fuel mass. Conversely, the BRM directly measures the instantaneous fuel mass, and the burn rate is computed by taking its derivative in time. This means that the two measurements can only be compared after either taking the integral or the derivative of one or the other. Fuel burn rate and mass are plotted for each fuel in Fig. 12, where fuel types are indicated on the right-hand side. The red dashed line is from the direct measurement of mass (BRM) and the black line corresponds to the values derived from the emissions data. For clarity, every hundredth data point is plotted for both data sets.

The general trend of the burn rate for all three fuels is the same; there is an increase in the burn rate at the beginning of the run, it peaks

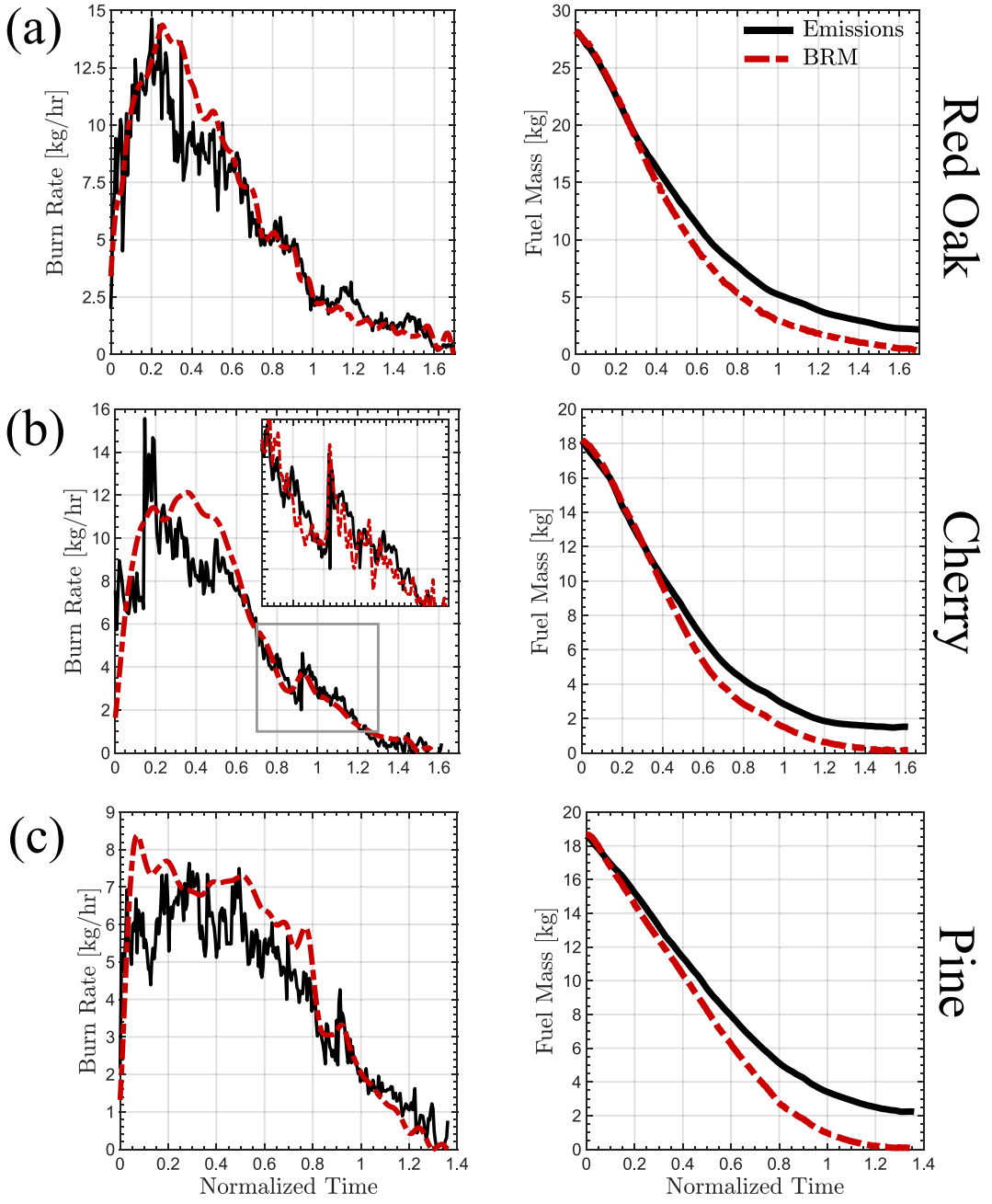

Fig. 12. Red oak (top row), cherry (middle row), and pine (bottom row) mass loss rate/burn rate (first column) and fuel mass (second column). Direct, intrusive measurements are shown in dash-dot red (burn rate monitor), while emissions-derived, non-intrusive measurements are shown in solid black. (For interpretation of the references to color in this figure legend, the reader is referred to the Web version of this article.)

between $t_n = 0.2$ and $t_n = 0.4$, and then steadily decreases until there is no fuel left at the end of the run. The run time for the red oak fuel is the longest ($t_n \approx 1.65$), while the run time for pine is the shortest ($t_n \approx 1.3$). The large fluctuations early in the run for the emissions burn rate data is a result of the variation in the computed carbon-normalized atomic values (Fig. 10). The full-resolution data sets for both measurements are shown in Fig. 12 (b) inset for cherry. The emissions and BRM data are completely decoupled, yet both data traces display the same minute fluctuations.

The BRM provides a direct measurement of the fuel mass by using the weight of the hanging basket to tare the load cell, and its uncertainty due to the load cell is ±0.14 kg. The fuel burn rate from the emissions data is integrated in time to compute the instantaneous fuel mass. The mass of the fuel is weighed prior to a run (with kindling included) to provide a mass anchor point for the emissions measurements, since the emissions-based measurements only give a change in mass, not an absolute mass. This eliminates the need for an appliance scale, since the fuel charge can always be weighed before a run. The second column in Fig. 12 shows a comparison between the BRM and emissions instantaneous fuel mass. In the initial portion of the run when the fuel burn rate is increasing toward its peak value, the fuel mass data agrees well with the direct measurements (BRM). As the run progresses in the constant H/ O release phase, the emissions-computed fuel mass does not decrease as fast as the directly measured fuel mass. This can also be seen from the burn rate curves, where the emissions data are lower in magnitude than the BRM data. To quantify the relative error (RE) between the emissions measurement and the direct measurement, a percent difference is calculated by dividing the difference between the emissions and BRM data by the initial fuel mass at the beginning of the run, as shown in Eq. (7).

$$\mathrm{RE}(t) = \frac{|m_{\mathrm{emissions}}(t) - m_{\mathrm{BRM}}(t)|}{m_{\mathrm{initial}}} \times 100 \tag{7}$$

The average relative percent error over the run duration for the three fuels are 5.4% for red oak, 5.4% for cherry, and 8% for pine (statistics are not provided in this study due to the limited number of runs). While some sources of uncertainty have been quantified, others need further investigation: non-homogeneous concentrations along the absorbing path length and at the Testo probing location, temperature non-uniformity in the flue gas, influence of particulate matter and unburned hydrocarbons, and the consequences of the complete combustion assumption inherent in the model formulation, to name a few.

At the end of the runs for each fuel type, the BRM measures a fuel mass near 0 kg, as would be expected for a complete burn of all the fuel. However, this method of mass measurement does not take into account fuel that had fallen through, or out of, the hanging basket during a run. It is typical to find small pieces of char on the floor of the primary chamber and a layer of ash on the floor of the secondary chamber. After a run, when the WHH has been allowed to cool down sufficiently, a vacuum is used to remove all material left over from the run that has accumulated in the primary and secondary chamber. This material is subsequently weighed to obtain the percentage of the fuel not able to exit through the flue, and thus not taken into account in the emissions measurements. Typically, the remaining products in the WHH from all three fuel types have a mass of approximately 0.5 kg, varying slightly from run to run. Based on the model formulation from Section 2, soot, particulate matter, and unburned hydrocarbons are not accounted for in this analysis. When these exit the flue of the WHH, they are not detected by the emission measurements, and thus result in unaccounted mass loss which manifest throughout the run, resulting in the final mass discrepancy between the emissions-based measurement and the BRM measurement seen in the right column of Fig. 12. While particulate matter emission factors can vary by a large margin based on fuel type, WHH operating conditions, and time during a run, using typical values (10 g·kg^{-1} to 50 g·kg^{-1}) [13, 42] can account for a reasonable amount of the difference between final measured fuel mass values. The methodology and measurements detailed in this study can thus provide a reliable supplemental measurement technique for the burn rate and fuel mass during typical WHH heating cycles/runs, which can further aid in the process of testing appliances to ensure their adherence to regulatory standards.

5. Conclusion

In this study, a methodology was introduced to use only flue gas emission measurements and air mass flow rate to calculate a high sensitivity, non-intrusive mass loss rate, which was then used to infer the instantaneous fuel mass during a run. Fuel mass is used in WHH regulatory standards testing in order to compute input energy content. Directly measuring the solid fuels in these WHH units is generally performed by weighing the entire appliance. The following major conclusions are drawn from the results of this study:

1. Using measurements of five emissions species (O_2, CO, NO, CO_2, H_2O), the time varying fuel composition ($CH_{x(t)}O_{y(t)}N_{z(t)}$) can be computed. With the addition of a measurement of air mass flow rate ($\dot{m}_a(t)$) into the WHH, the fuel mass loss rate ($\dot{m}_f(t)$) is calculated, and then integrated in time to compute the instantaneous fuel mass during a run ($m_f(t)$).

2. After the drying stage of a run, the H and O are driven from the fuel in the pyrolysis/combustion stage at roughly the same rate until all the fuel H and O are released. The mean release ratio of $\mu = \mathrm{H/O}$ was very near the previously assumed value of 2, validating that assumption. This means that if CO_2 and H_2O emission measurements cannot be made, a reasonable assumption of $\mu = 2$ may be made to still obtain reasonable values of the fuel mass loss rate and fuel mass.

3. The benefits of the emissions-based fuel mass measurement are that it is non-intrusive and provides similar accuracy and precision as a full-appliance scale, indicating that this method can be used as further validation of the established methods for computing mass loss during certification of these appliances.

A single run for each fuel was presented in this study. Future repeat measurements for each fuel type will allow for statistics to be computed, and run-to-run variability characterized. Different fuel types, fuel dimensions, and loading configurations should also be tested, and the method validated further to ensure that none of these variables change the accuracy and precision of the measurement technique. Finally, an ultimate analysis of the fuel types should be performed, and the H/O ratio compared to the mean release ratio to ensure consistent results. This technique has the potential to be a useful method of measuring fuel mass non-intrusively, while providing both the accuracy and precision of current techniques, and can aid in the testing of appliances to satisfy the regulatory standards.

Acknowledgments

Support has been provided in part by National Science Foundation (NSF) under grant number #1704447. This work was also supported by the New York State Energy Research and Development Authority (NYSERDA) under contract number #32966 (Ms. Megan Bulman, Mr. Michael Genovese, and Dr. Ellen Burkhard). We would like to thank Ms. Victoria Miller at Summit Wood Industries for their supply of the BIO-BLOCKS® fuel used in this study, and Mr. Dale Furman and Mr. Mark Odell from Econoburn for their generous donation of the EBW-200 wood-fired WHH. We would also like to thank Dr. Ron Parker for his help with the laser diagnostic experiments and Mr. Xinnan Peng and the University at Buffalo Engineering Machine Shop for their support in constructing the instrument modifications to the WHH and flue.

References

[1] E. Rehfuess, et al.. Fuel for Life: Household Energy and Health, World Health Organization, 2006.

[2] P. McKendry, Energy production from biomass (part 1): overview of biomass, Bioresource Technology 83 (1) (2002) 37–46, https://doi.org/10.1016/S0960-8524(01)00118-3.

[3] A. Demirbas, Combustion characteristics of different biomass fuels, Progress in Energy and Combustion Science 30 (2) (2004) 219–230, https://doi.org/10.1016/j.pecs.2003.10.004.

[4] J. Lehmann, A handful of carbon, Nature 447 (7141) (2007) 143–144, https://doi.org/10.1038/447143a.

[5] Varun, I.K. Bhat, R. Prakash, LCA of renewable energy for electricity generation systems - A review, Renewable and Sustainable Energy Reviews 13 (5) (2009) 1067–1073, https://doi.org/10.1016/j.rser.2008.08.004.

[6] H. Lund, B. Möller, B.V. Mathiesen, A. Dyrelund, The role of district heating in future renewable energy systems, Energy 35 (3) (2010) 1381–1390, https://doi.org/10.1016/j.energy.2009.11.023.

[7] T. Levander, S. Bodin, Controlling Emissions from Wood Burning, Technology Report (2014), https://doi.org/10.6027/TN2014-517.

[8] Z. Chafe, M. Brauer, M.-E. Héroux, Z. Klimont, T. Lanki, R.O. Salonen, K.R. Smith, Residential heating with wood and coal: health impacts and policy options in Europe and North America. Technology Report, World Health Organization, 2015.

[9] B.D. Smith, Nordic Energy Technology Perspectives 2016, Nordic Energy Research, 2016.

[10] T. Butcher, N. Russell, Review of EPA Method 28 Outdoor Wood Hydronic Heat Test Results, Final Report, New York State Energy Research and Development Authority (NYSERDA), 2011.

[11] Environmental Protection Agency, Method 28 - Certification and Auditing of Wood Heaters, Technology Report, Environmental Protection Agency, 2017.

[12] CSA Group, Technology Report, in: Performance Testing of Solid-Fuel-Burning Heating Appliances, Canadian Standards Association, 2015.

[13] J.S. Kinsey, A. Touati, T.L.B. Yelverton, J. Aurell, S.-H. Cho, W.P. Linak, B. K. Gullett, Emissions characterization of residential wood-fired hydronic heater technologies, Atmospheric Environment 63 (2012) 239–249, https://doi.org/10.1016/j.atmosenv.2012.08.064.

[14] T. Butcher, R. Trojanowski, C. Brown, G. Wei, Report on Testing of the Econoburn Model EBW200-170 Wood Hydronic Heater using Partial Thermal Storage, Tech Report, Brookhaven National Laboratory, 2014.

[15] T. Butcher, Technical Report, in: Effect of Thermal Storage on the Performance of a Wood Pellet-fired Residential Boiler, Brookhaven National Laboratory, 2017.

[16] P. Ovchinnikov, A. Borodiņecs, K. Strelets, Utilization potential of low temperature hydronic space heating systems: A comparative review, Building and Environment 112 (2017) 88–98, https://doi.org/10.1016/j.buildenv.2016.11.029.

[17] G. Martinopoulos, K.T. Papakostas, A.M. Papadopoulos, A comparative review of heating systems in EU countries, based on efficiency and fuel cost, Renewable and Sustainable Energy Reviews 90 (2018) 687–699, https://doi.org/10.1016/j.rser.2018.03.060.

[18] R. Trojanowski, V. Fthenakis, Nanoparticle emissions from residential wood combustion: A critical literature review, characterization, and recommendations, Renewable and Sustainable Energy Reviews 103 (2019) 515–528, https://doi.org/10.1016/j.rser.2019.01.007.

[19] P. Glarborg, A.D. Jensen, J.E. Johnsson, Fuel nitrogen conversion in solid fuel fired systems, Progress in Energy and Combustion Science 29 (2) (2003) 89–113, https://doi.org/10.1016/S0360-1285(02)00031-X.

[20] M. Rabaçal, U. Fernandes, M. Costa, Combustion and emission characteristics of a domestic boiler fired with pellets of pine, industrial wood wastes and peach stones, Renewable Energy 51 (2013) 220–226, https://doi.org/10.1016/j.renene.2012.09.020.

[21] K. Sartor, Y. Restivo, P. Ngendakumana, P. Dewallef, Prediction of SO_x and NO_x emissions from a medium size biomass boiler, Biomass and Bioenergy 65 (2014) 91–100, https://doi.org/10.1016/j.biombioe.2014.04.013.

[22] W. Wagner, A. Pruss, International Equations for the Saturation Properties of Ordinary Water Substance. Revised According to the International Temperature Scale of 1990. Addendum to J. Phys. Chem. Ref. Data 16, 893 (1987), Journal of Physical and Chemical Reference Data 22 (3) (1987) 783–787, https://doi.org/10.1063/1.555926.

[23] SFPE, SFPE Handbook of Fire Protection Engineering, 5th, National Fire Protection Agency, 2016.

[24] D.K. Shen, S. Gu, K.H. Luo, A.V. Bridgwater, M.X. Fang, Kinetic study on thermal decomposition of woods in oxidative environment, Fuel 88 (6) (2009) 1024–1030, https://doi.org/10.1016/j.fuel.2008.10.034.

[25] R. García, C. Pizarro, A.G. Lavín, J.L. Bueno, Characterization of Spanish biomass wastes for energy use, Bioresour. Technol. 103 (1) (2012) 249–258, https://doi.org/10.1016/j.biortech.2011.10.004.

[26] G. Ionescu, C. Bulmău, Estimation of Energy Potential for Solid Pyrolysis By-Products Using Analytical Methods, in: P. Kusch (Ed.), Analytical Pyrolysis, IntechOpen, 2019.

[27] C. Ryu, Y.B. Yang, A. Khor, N.E. Yates, V.N. Sharifi, J. Swithenbank, Effect of fuel properties on biomass combustion: Part I. Experiments - fuel type, equivalence ratio and particle size, Fuel 85 (7–8) (2006) 1039–1046, https://doi.org/10.1016/j.fuel.2005.09.019.

[28] E. Pettersson, C. Boman, R. Westerholm, D. Boström, A. Nordin, Stove Performance and Emission Characteristics in Residential Wood Log and Pellet Combustion, Part 2: Wood Stove, Energy and Fuels 25 (1) (2011) 315–323, https://doi.org/10.1021/ef100774x.

[29] H. Filipe dos Santos Viana, A. Martins Rodrigues, R. Godina, J. Carlos de Oliveira Matias, L. Jorge Ribeiro Nunes, Evaluation of the Physical, Chemical and Thermal Properties of Portuguese Maritime Pine Biomass, Sustainability 10 (8) (2018), https://doi.org/10.3390/su10082877.

[30] B.M. Jenkins, L.L. Baxter, T.R. Miles Jr., T.R. Miles, Combustion properties of biomass, Fuel Processing Technology 54 (1–3) (1998) 17–46, https://doi.org/10.1016/S0378-3820(97)00059-3.

[31] J.P. Richter, J.M. Weisberger, J.C. Mollendorf, P.E. DesJardin, Emissions from a domestic two-stage wood-fired hydronic heater: Effects of non-homogeneous fuel decomposition, Renewable Energy 112 (2017) 187–196, https://doi.org/10.1016/j.renene.2017.05.038.

[32] J.P. Richter, B.T. Bojko, J.C. Mollendorf, P.E. DesJardin, Measurements of fuel burn rate, emissions and thermal efficiency from a domestic two-stage wood-fired hydronic heater, Renewable Energy 96 (Part A) (2016) 400–409, https://doi.org/10.1016/j.renene.2016.04.096.

[33] J.P. Richter, J.C. Mollendorf, P.E. DesJardin, Absolute and relative emissions analysis in practical combustion systems - effect of water vapor condensation, Measurement Science and Technology 27 (11) (2016), https://doi.org/10.1088/0957-0233/27/11/117002.

[34] M.F. Modest, Chapter 11 - Radiative Properties of Molecular Gases. Radiative Heat Transfer, 3rd, Academic Press, 2013, pp. 303–386.

[35] I.E. Gordon, L.S. Rothman, C. Hill, R.V. Kochanov, Y. Tan, P.F. Bernath, M. Birk, V. Boudon, A. Campargue, K.V. Chance, B.J. Drouin, J.-M. Flaud, R.R. Gamache, J. T. Hodges, D. Jacquemart, V.I. Perevalov, A. Perrin, K.P. Shine, M.-A.H. Smith, J. Tennyson, G.C. Toon, H. Tran, V.G. Tyuterev, A. Barbe, A.G. Császár, V.M. Devi, T. Furtenbacher, J.J. Harrison, J.-M. Hartmann, A. Jolly, T.J. Johnson, T. Karman, I. Kleiner, A.A. Kyuberis, J. Loos, O.M. Lyulin, S.T. Massie, S.N. Mikhailenko, N. Moazzen-Ahmadi, H.S.P. Müller, O.V. Naumenko, A.V. Nikitin, O.L. Polyansky, M. Rey, M. Rotger, S.W. Sharpe, K. Sung, E. Starikova, S.A. Tashkun, J. Vander Auwera, G. Wagner, J. Wilzewski, P. Wcisło, S. Yu, E.J. Zak, The HITRAN2016 molecular spectroscopic database, Journal of Quantitative Spectroscopy & Radiative Transfer 203 (2017) 3–69, https://doi.org/10.1016/j.jqsrt.2017.06.038.

[36] J.M. Weisberger, J.P. Richter, R.A. Parker, P.E. DesJardin, Direct absorption spectroscopy baseline fitting for blended absorption features, Applied Optics 57 (30) (2018) 9086–9095, https://doi.org/10.1364/AO.57.009086.

[37] J.M. Weisberger, P.E. DesJardin, Sensitivity of Blended Baseline Fitting Method for Direct Absorption Spectroscopy, AIAA Aviation 2019 Forum, 2019.

[38] C.S. Goldenstein, V.A. Miller, R.M. Spearrin, C.L. Strand, SpectraPlot.com: Integrated spectroscopic modeling of atomic and molecular gases, Journal of Quantitative Spectroscopy and Radiative Transfer 200 (2017) 249–257, https://doi.org/10.1016/j.jqsrt.2017.06.007.

[39] K. Sun, X. Chao, R. Sur, C.S. Goldenstein, J.B. Jeffries, R.K. Hanson, Analysis of calibration-free wavelength-scanned wavelength modulation spectroscopy for practical gas sensing using tunable diode lasers, Measurement Science and Technology 24 (12) (2013), https://doi.org/10.1088/0957-0233/24/12/125203.

[40] ASME, Measurement of Fluid Flow in Pipes Using Orifice, Nozzle, and Venturi, Technology Report ASME MFC-3M-2004, American Society of Mechanical Engineers, 2004.

[41] J.P. Richter, J.M. Weisberger, B.T. Bojko, J.C. Mollendorf, P.E. DesJardin, Numerical modeling of homogeneous gas and heterogeneous char combustion for a wood-fired hydronic heater, Renewable Energy 131 (2019) 890–899, https://doi.org/10.1016/j.renene.2018.07.087.

[42] S. Simões Amaral, J. Andrade de Carvalho, M.A. Martins Costa, C. Pinheiro, Particulate Matter Emission Factors for Biomass Combustion, Atmosphere 7 (11) (2016), https://doi.org/10.3390/atmos7110141.